Article

Fused Filament Fabrication of WC-10Co Hardmetals: A Study on Binder Formulations, and printing variables.

Julián David Rubiano Buitrago *, Andrés Fernando Gil Plazas, Luis Alejandro Boyacá Mendivelso, Liz Karen Herrera Quintero

Posted Date: 10 May 2024

doi: 10.20944/preprints202405.0642.v1

Keywords: Hardmetals; Fused Filament Fabrication; Additive Manufacturing; Feedstock Formulation; Printing Force Measurement.

 doi:10.20944/preprints202405.0642.v1

Article

Fused Filament Fabrication of WC-10Co Hardmetals: A Study on Binder Formulations, and Printing Variables

Julián David Rubiano Buitrago [1,*], Andrés Fernando Gil Plazas [2], Luis Alejandro Boyacá Mendivelso [3] and Liz Karen Herrera Quintero [1]

[1] Department of Mechanical and Mechatronics Engineering, Faculty of Engineering, National University of Colombia, Bogotá, Colombia; judrubianobu@unal.co (J.D.R.B), lkherreraq@unal.edu.co (L.K.H.Q).
[2] Materials and Testing Center, National Learning Service-SENA, Bogotá, Colombia; agilp@sena.edu.co (A.F.G.P)
[3] Department of Chemical and Environmental Engineering Faculty of Engineering, National University of Colombia, Bogotá, Colombia; laboyacam@unal.edu.co (L.A.B.M)
* Correspondence: judrubianobu@unal.co

Abstract: This research investigates the application of Fused Filament Fabrication (FFF) in producing WC-10Co hardmetals, focusing binder formulations and understanding its influence on extrusion force and the influence of printing variables on green density of the samples. By examining the interplay between different binder compositions and backbone contents, the study aims to enhance the mechanical properties of the sintered parts while reducing defects inherent in the printing process. Evidence suggested that formulated feedstocks influenced the hardness of the sintered hardmetal, not due to microstructural changes but to macrostructural responses like macro defects introduced during printing, debinding and sintering of the samples. The results demonstrate the critical role of PP-MA content in improving part density and sintered hardness, suggesting the need for specific thermal debinding protocols tailored to each feedstock. The study provides insights into the formulation of feedstocks for hardmetal FFF, proposing a path toward refining manufacturing processes for better quality and performance of 3D printed hardmetal components.

Keywords: Hardmetals; Fused Filament Fabrication; Additive Manufacturing; Feedstock Formulation; Printing Force Measurement

1. Introduction

Since the inception of sintered tungsten carbide cobalt (WC-Co) hardmetal by Karl Schröter in the 1920s, the quest among researchers and manufacturers to develop more efficient and cost-effective production methods for hardmetals with improved properties and intricate geometries has been ongoing. Also known as cemented carbides, hardmetals are composite materials of hard, brittle WC grains embedded within a soft, ductile metallic matrix, typically composed of Co, Fe, or Ni. Moreover, hardmetals often include additional carbides like TiC, TaC, Cr3C2, NbC, or Mo2C, which serve as inhibitors of WC-grain growth [1–3]. WC-10Co hardmetals are highly valued for their exceptional hardness and toughness, qualities that render them ideal for producing tools subjected to heavy impact and wear. These applications include the manufacturing devices like anvils, cutters, slitters, drills, as well as tools used in cold-working and mining [4].

Additive manufacturing (AM) offers a compelling alternative for producing WC-Co components, notable for its ability to create new geometries and cost-effectively produce small batches. Notably, AM allows for incorporating the complex features without increasing production costs, leading to its characterization as a "complexity for free" process [5]. Additive Manufacturing technologies for hardmetals include beam-based methods like Directed Energy Deposition (DED), Laser Engineering Net Shaping (LENS)[6], Direct Laser Fabrication (DLF)[7], Selective Laser Sintering (SLS) [8,9], Selective Laser Melting (SLM) [10], which sequentially produce each hardmetal layer and managing anisotropy variations is a key challenge. In contrast, beamless methods like Fused Filament Fabrication (FFF), Composite Extrusion Manufacturing (CEM), Binder Jetting (BJ),

 doi:10.20944/preprints202405.0642.v1

and 3D gel/direct-ink-write/robo-casting use a mix of powders and binder systems[11]. Indeed, in beamless methods, so-called "green parts" are constructed layer by layer. However, these parts require further post-treatment processes. This involves the removal of the binder or debinding and a sintering step, both essential to achieving the final, fully structured part with desired physical and mechanical properties [12]. Beamless methods tend to produce microstructures with lower residual stresses since the entire part is sintered simultaneously [11,13], and overcome the new layer cooling dynamics of beam-based AM methods [14].

The material extrusion process, specifically for polymeric filaments, was first patented by Stratasys [15] under the trademark Fused Deposition Modelling or (FDM™). Later, the term Fused Filament Fabrication (FFF), was introduced as an open, non-registered name for the technology [16]. Influenced by Powder Injection Molding (PIM), FFF was adapted to shape metals, ceramics, and composites in a three-step process: Shaping (by PIM or FFF), Debinding (solvent and/or thermal), and Sintering (SDS) [17,18]. Pioneering research by Agarwala, et al. [19] led to the first binder system developed for the FFF processing of Si_3N_4 parts. Subsequent studies highlighted the necessity for tailored binder systems for different powdered materials [20].

In FFF, the filament serves dual purposes as the extrusion driver and the extruded material. If the viscosity of the filament is too high or its strength too low, the feedstock can become unprintable, often failing due to buckling [21]. Additionally, the filament must withstand spooling processes and when printed, the part must support internal pressure generated during solvent and thermal debinding, which might cause defects like cracking and blistering [22,23]. Styrene-ethylene/butylene-styrene (SEBS) thermoplastic elastomers have been effective in FFF binder formulations due to their flexibility and solubility in the first debinding stage [24–27]. When working with submicrometric particles, adding Paraffin Wax to SEBS in the binder system can effectively modulate viscosity and facilitate the debinding [28].

Polyolefins such as Polypropylene and Polyethylene are commonly used as backbone materials. Nevertheless materials such as EVA and PLA have been reported [28]. MCNulty, et al. [29] developed binder systems for the FFF of Lead zirconate titanate (PZT) samples, utilizing polyolefins and Hydrocarbon resin. Their research demonstrated the potential of adapting commercially available materials to create FFF-compatible feedstocks. Various research efforts, including those by Cano et al. [30] ZrO2 and Momeni et al. [31] for Al, have focused on using grafted and non-grafted polyolefins as backbones in FFF feedstocks. These studies revealed improvements in powder dispersion and rheological behavior, accompanied by a slight increase in the viscosity of the feedstocks. Lengauer, et al. [32] successfully printed, debinded, and sintered WC-10Co and Ti(C,N)-Co/Ni-based Cermets using TPE as a soluble polymer and PP functionalized with maleic anhydride. They highlighted the need for optimized printing strategies to achieve defect-free microstructures, which aligns with Agarwala et al. [33] who developed printing strategies to rectify defects in Si_3N_4 and 17-4ph stainless steel (SS) printed by FFF.

Additionally, Agarwala et al. [34] crafted unique binder systems for WC-Co, SiO_2, 17-4 PH SS, Si_3N_4, and Al2O3, observed that smaller particle sizes in the same binder system, due to their increased surface area, led to higher viscosity in the feedstocks, prompting the need for reformulations incorporating different surfactants in the binder system to manage this challenge. Surfactants based on fatty acids with long carbon chains, such as Stearic Acid (SA) are effective for WC-Co in polymeric binders, as demonstrated in different studies [35,36]. The feedstock's viscosity, the liquefier system's geometrical factors, and the layer height have been modeled to relate them with the extrusion force of ABS and PLA [37,38] alloying to describe it with the final properties of the printed material.

This study will investigate various binder formulations for WC-10Co in Fused Filament Fabrication (FFF), focusing on how binder composition and backbone content impact the printing force, the emergence of green part defects and their dependence on the printing parameters, and their effects on the microstructure and hardness of sintered hard metals.

2. Materials and Methods

2.1 Materials:

 doi:10.20944/preprints202405.0642.v1

This study employed hardmetal ready-to-press powders, consisting of 10 wt% cobalt (Co) and a balance of tungsten carbide (WC). These powders were agglomerated using a spray drying process with an addition of 1 wt% paraffin wax, supplied by ZCC (China). The binder systems included a combination of both soluble and non-soluble polymers. The soluble components comprised Thermoplastic Elastomer TPE (Sungallon, China), Paraffin Wax (PW) as a viscosity modulator (Panreac), and Stearic Acid (SA) as a surfactant (Sigma Aldrich). Additionally, the system incorporated a mixture of Polypropylene Random-Copolymer (PP) (Essentia, Colombia) and Polypropylene Grafted with Maleic Anhydride (PP-MA), which served as the backbone.

We prepared four different formulations to investigate the impact of the backbone's content and composition on the feedstocks. We varied the backbone composition using ratios of PP-MA to PP at 3:2 and 2:3. Additionally, we used two distinct backbone contents in the binder system: 26 wt% and 31 wt%. To offset the variations in backbone content, we added additional TPE. Throughout the experiment, we kept both SA and PW constant (See Table 1).

Table 1. Formulated binder Systems (52%vol) to be mixed with 48%vol WC-Co powders.

Binder	PP-MA	PP	TPE	PW	SA
	%wt.	%wt.	%wt.	%wt.	%wt.
M1	18.62	12.42	46.56	18,00	4.40
M2	15.60	10.40	51.60	18.00	4.40
M3	12.42	18.62	46.56	18.00	4.40
M4	10.40	15.60	51.60	18.00	4.40

[1] The PW content of the RTP powder is included in the binder calculation.

The feedstocks were prepared using a shear-based mixing apparatus. Initially, the polymers underwent a homogenization process for 10 minutes. This process was followed by the gradually adding powders into the molten mixture, executed in three distinct stages. The mixture was then continuously mixed for 60 minutes at a temperature of 160 °C. After mixing, the feedstocks were cut into small pieces, each measuring less than 5 mm in every dimension. These fragments were used to produce filament, employing a single-screw extruder with a 1.75 mm diameter die, operating at 180°C. To assess the changes in the binder system resulting from the powder addition, 50g of each binder type was mixed. However, the powder-free samples were subjected to an identical homogenization duration of 60 minutes to ensure a standardized comparison. To distinguish between the samples, 'M' without the suffix 'P' will denote the binder system alone, while 'M+P' will indicate the binder system mixed with the hardmetal powder.

2.2. Thermal Properties

The thermal properties of the feedstocks and the binder systems were analyzed using Differential Scanning Calorimetry (DSC) (Mettler Toledo). The materials were incrementally heated from room temperature to 250°C at a rate of 10 °C/min, under a nitrogen flow of 50ml/min. The crystallinity degree of each virgin polymer, binder system, and feedstock was calculated using the formula [39]:

$$X_c = \frac{\Delta H_m}{\Delta H_m^0 * w} \quad (1)$$

Where ΔH_m represents the fusion enthalpy (derived from the integral of the endothermic peak on the DSC curve), and ΔH_m^0 is the enthalpy of fully crystalized PP (207 J/g) [40], and w is the weight fraction of PP in the analyzed sample.

To evaluate the thermal stability of both the binder systems and the feedstocks, a Thermogravimetric Analysis (TGA) (Mettler Toledo). The samples were heated up to 700 °C at a rate of 10 °C/min under a nitrogen flow of 50.0 ml/min. During this process, the samples' weight and the rate of weight loss were measured.

2.3. Printing Force Measurements

A custom-built Arduino-based device was employed to measure the extrusion force of each filament. Equipped with two 5 kg load cells, this device featured a mechanism to maintain the FFF

 doi:10.20944/preprints202405.0642.v1

extrusion system's alignment and isolate it from the pulling motor. The filaments were tested at extrusion speeds of 7.5 and 10 mm/s, and at temperatures of 200, 210, and 220°C and 20 cm of tested material in each run. Each experimental setup was replicated three times, with the resulting data being collected at a frequency of 0.2 Hz, for further analysis to calculate the average extrusion force. The nozzle had a diameter of 0.6 mm, and the extrusion system was configured to mimic the standard FFF machine used in the printing experiments. The systematic error in measuring the extrusion force was determined to be less than 0.2N. Care was taken to use 1.75mm filaments to avoid error due to the higher transversal area of any filaments.

2.4. Printing

An Ender 3 V2 FFF printer, specifically modified to include a direct extrusion drive system, was used to shape cylindrical samples with a diameter of 17 mm and a height of 7 mm. Five samples were printed at three different printing temperatures for each feedstock: 200, 210, and 220°C for 80 samples (60 printed at 10 mm/s and 20 additional printed at 7.5mm/s). The layer thickness and nozzle diameter settings were maintained at 0.3 mm and 0.6 mm, respectively. A printing flow of 103% was used for all the samples.

Table 2. Key Printing Parameters Utilized.

Infill Pattern	Number of External Lines	Infill Overlap	Retraction	Bed Temperature	Cooling fan
Lines	1	50%	No	95 °C	Off

2.5. Debinding and Sintering

After printing the samples were immersed in cyclohexane for 72 h to remove the soluble polymers. Next, a vacuum furnace performed the thermal debinding and sintering in one single step. Considering the focus of this study does not extend to the macro-scale analysis of sintering and debinding stages, a non-optimized thermal debinding cycle was utilized, featuring a heating rate of 0.2 °C/min between 400 and 550 °C, next a sintering plateau of 60 minutes at 1500°C was employed for final densification of the samples. The sintering process for the samples was conducted within graphite containers to prevent decarburization, using an argon atmosphere for protection.

2.5. Characterization

The density of the printed and sintered samples was determined using the Archimedes method, with 99.9% ethanol employed to enhance the wetting of the sample surfaces. To identify various defects after printing and correlate them with the feedstocks and printing temperatures used, a cryogenic 3-point bending test was conducted on one sample from each feedstock configuration. The test setup involved placing the samples on two rods, each 10 mm in diameter, spaced 14 mm apart at their centers. A third rod of the same diameter was advanced at a 1 mm/min rate until the sample fractured. Before testing, the green samples were immersed in liquid nitrogen for 10 minutes to ensure uniform internal temperature. After sintering, the samples were sectioned, subjected to diamond polishing for a smooth finish, and then analyzed. Both light-optical microscopy (OM) (Zeiss Z1.m) and Scanning Electron Microscopy (SEM) (Phenom XL) were used to examine the green and sintered samples closely. The Digital Image software ImageJ™ was utilized for analyzing SEM micrographs to measure the grain size.

3. Results and Discussion

3.1. Thermal Properties

3.1.1. DSC Analysis

The DSC thermograms of the raw materials, binder systems and feedstocks, are shown in Figure 1. The unmodified polypropylene (PP) has a notably lower melting point compared to polypropylene

 doi:10.20944/preprints202405.0642.v1

grafted with maleic anhydride (PP-MA). This difference is highlighted by two distinct fusion peaks in the PP curve, attributed to the melting of co-monomers added to enhance the polymer fluidity, with the second peak representing the complete melting of the polymeric chain, including the propylene co-monomer. Interestingly, the thermoplastic elastomer (TPE) shows a minor endothermic reaction at 62°C, which vanishes upon integration into the feedstocks. The DSC thermograms' data, including the melting temperature T_m, fusion enthalpy ΔH_m, start and end temperatures of the melting reaction, and degree of crystallinity derived from Equation 1, are quantitatively summarized in Table 2. While the feedstocks and binder systems displayed negligible variations in melting points, a pronounced influence of the fusion enthalpy was observed relative to the backbone content and the presence of PP-MA. This indicates that a mere 5% substitution of the backbone with TPE fosters a significant interaction between the PP and TPE chains and diminishes their crystallization capability, thereby impacting their fusion enthalpy.

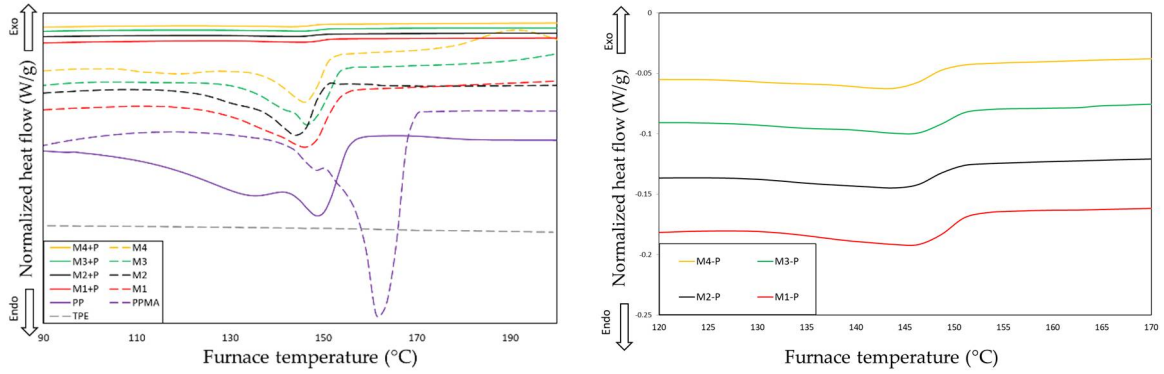

Figure 1. DSC curves of a) Raw polymers, binder systems and binder systems mixed with WC-10Co powders, b) Magnification of the binder systems mixed with the powders.

The crystallinity of the feedstocks exhibited a pronounced dependence on the content of PP-MA. Notably, the M1 sample, characterized by the highest PP-MA concentration, uniquely demonstrated increased crystallinity upon integration with powders. This contrasts with the behavior of the other mixtures (M2, M3, and M4), which, despite varying levels of PP-MA content, all experienced a decrease in crystallinity following the addition of WC-10Co powder. The enhancement in crystallinity within a polymeric matrix due to powder addition is attributed to the creation of multiple nucleation sites [39]. The lack of increased crystallinity in mixtures M2, M3, and M4 underscores the critical role of surface interactions between the powder and the polymer matrix in the nucleation process, significantly influenced by the non-polar characteristics of PP. The onset and endset temperatures of the melting process are influenced by the amount of PP-MA in the mixture, suggesting an interaction between the polar properties of PP-MA and the powder surfaces.

Table 3. Calculated data.

Description	T_m [$C°$]	T onset [$C°$]	T endset [$C°$]	ΔH_m $\left[\frac{J}{g}\right]$	X_c [%]
PP	148.59	133.5	155.7	91.03	43.98%
PP-MA	161.05	153.7	168.5	105.18	50.81%
TPE	-			-	-
M1	145.93	123.76	153.54	41.19	54.32%
M1+P	145.63	128.18	151.51	1.72	43.20%
M2	144.22	130.40	149.86	29.33	46.24%
M2+P	144.43	123.42	150.32	1.04	31.20%
M3	145.76	135.56	153.74	32.46	45.25%
M3+P	145.69	125.76	151.48	0.88	22.07%

 doi:10.20944/preprints202405.0642.v1

M4	146.06	133.25	151.68	18.23	28.76%
M4+P	143.59	126.31	149.55	0.83	24.77%

3.1.2. TGA Analysis

The degradation profiles of the raw materials, as evidenced in the TGA analysis presented in Figure 2-a, reveal distinct rates and temperatures of thermal decomposition The PP-MA exhibits an onset of degradation at lower temperatures relative to PP, likely attributable to the incorporation of Maleic Anhydride. Notably, the thermal decomposition residuals at 700°C for PP and PP-MA are 0.029% and 0.19%, respectively. This disparity suggests that feedstocks with a higher proportion of PP-MA could have a pronounced impact on the carbon content in the final printed samples due to incomplete combustion. Moreover, the M1-P sample, enriched with PP-MA, demonstrates a higher thermal degradation onset than other feedstocks. This observation may indicate a more robust interaction between the polar Maleic Anhydride component and the surfaces of the powders, as the proportion of the grafted backbone increases. Such interactions indicate enhanced thermal stability, which could benefit printed materials' performance under elevated temperatures.

The backbone content and the proportion of PP-MA within it had a discernible impact on the derivative mass change, as seen in Figure 2-b. It was observed that samples with a higher backbone content exhibited more significant rates of mass change. This, in turn, would translate to increased internal pressures within the part during the thermal debinding process. Furthermore, within the groups containing 31% (M1 and M3) and 26% (M2 and M4) backbone content, the degradation temperature varied following the presence of PP-MA. This variation suggests that the PP-MA component within the backbone may significantly influence the material's thermal stability and degradation behavior during processing. The feedstocks M2-P and M4-P exhibit a slight mass loss of 0.25% before reaching 200°C, likely due to the volatilization of low molecular weight additives contained within the used high fluidity PP, which are more predominant in these samples.

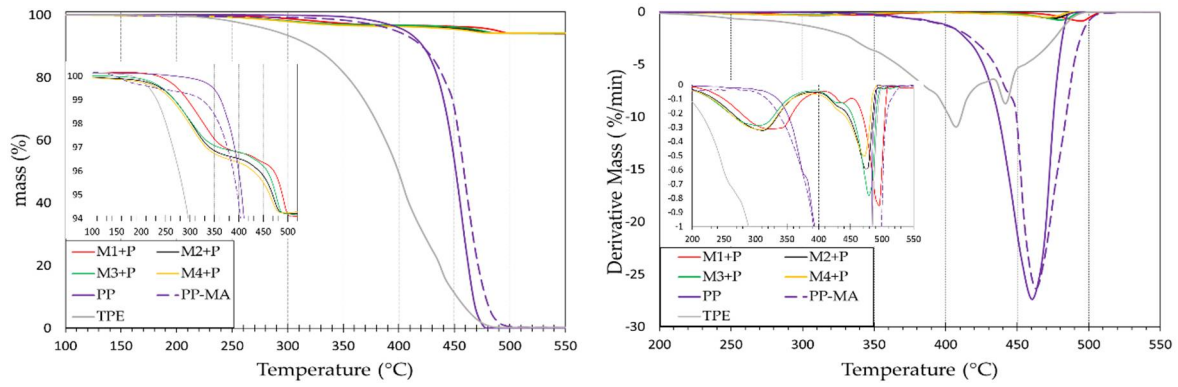

(**a**) (**b**)

Figure 2. TGA results of the studied feedstocks, a) Mass-loss temperature diagram, b) Derivative mass calculation.

3.2. Force Measurement Analysis

Various researchers have explored the rheology of powder mixtures with polyolefins and TPE [41]. Given the non-Newtonian behavior of these types of raw materials, it is understood that with an increase in shear rate, there is a reduction in viscosity [35]. However, in the practical context of FFF printing, the Extrusion Force as a response variable has been related to the sum of pressure drops in three areas: the start of the nozzle, the section change zone, and the capillary or nozzle exit zone, this dependency is influenced by geometric factors, rheological properties of the material, and mass flow [37,42]. Since these three zones were replicated identically to those in the printer within our force measurement device, the powder loading is constant, and the testing conditions are the same. Any increase or decrease in the measured printing force accurately reflects the material response of the manufactured filaments. In agreement with other authors, Figure 3 clearly shows that increasing the

 doi:10.20944/preprints202405.0642.v1

extrusion temperature is often suggested to reduce high filament viscosities, as this process lowers the printing force by boosting the mobility of the polymer chains.

The mean extrusion force for the four different feedstocks as a function of extrusion speed and nozzle temperature is illustrated in Figure 3-a. The analysis demonstrates that extrusion speed significantly impacts the extrusion force across all tested conditions. Despite the anticipated increase in shear rate with higher extrusion speeds, the 7.5 mm/s speed resulted in a lower extrusion force for all feedstocks and temperatures tested. Notably, the M4-P feedstock displayed the lowest extrusion force suggesting it had the lowest viscosity among all samples. This finding is consistent with the literature on non-grafted PP, which posits that the absence of grafting agents, such as maleic anhydride, might lead to decreased material viscosity, easing the extrusion process [43].

Conversely, the M1-P feedstock maintained an extrusion force below that of the 10mm/s speed and nearly identical to the 7.5mm/s conditions compared to the M2 and M3 samples. This variance may be attributed to enhanced powder dispersion facilitated by the higher PP-MA content, resulting in improved distribution within the polymer matrix. The M2-P and M3-P feedstocks exhibited higher extrusion forces at lower temperatures, with notable variability as the printing temperature increased. In contrast, the M1-P feedstock demonstrated the highest printing force at 220°C. This behavior could be explained by the robust particle-polymer interactions of PP-MA, as indicated by the TGA analysis.

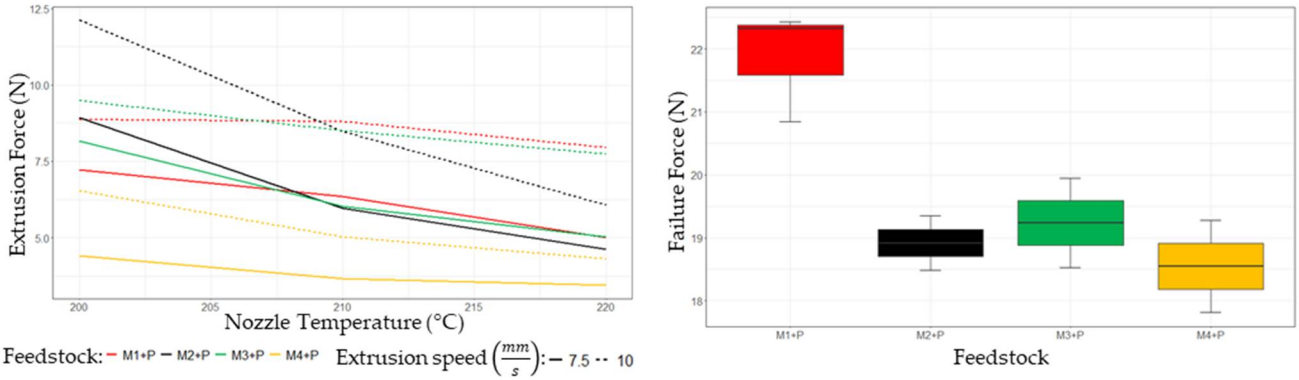

(**a**) (**b**)

Figure 3. Force measurements for manufactured feedstocks: (a) Variation with temperature and extrusion speed, (b) Test at ambient temperature leading to filament failure.

The maximum force or failure force of the developed filaments is reported in Figure 3-b. It can be observed that the M1-P sample exhibited significantly greater resistance than the other samples, which did not show significant differences compared . This outcome directly results from two factors: a better adhesion between the powders and the polymer matrix, attributed to the higher PP-MA content and a higher achieved crystallinity of the feedstock. Additionally higher load capacity also implies a lower probability of process failure, thereby enhancing reliability. However, the M2, M3, and M4 feedstocks demonstrated a load capability that required only a maximum of 50% of their failure force under the shown printing conditions. Their reduced capacity can be attributed to a higher content of TPE in the cases of M2 and M4 mixtures, and to a lower ratio of PP-MA/PP for the M2 sample. All filaments failed due to lateral abrasion caused by the pushing rollers of the FFF system. For productivity reasons and because the speed of 10 mm/s was significantly below the load capacity, this value was chosen for conducting the first run of printing experiments.

3.4. Samples Printed at 10 mm/s and Different Temperatures.

Following the measurement of green densities and the calculation of relative green densities, assumptions were tested, and a two-way ANOVA was conducted, revealing significant effects from both the printing temperature, feedstock and an interaction between the printing temperature and the feedstock, see Table 4. The findings depicted in Figure 4 align with the ANOVA results, demonstrating varied behavior in the relative green density across different feedstocks and printing

 doi:10.20944/preprints202405.0642.v1

temperatures. Samples closest to the median density were chosen for cryogenic three-point bending tests to analyze the internal defects of the samples. Figure 5 demonstrates samples printed at 200°C and 220°C post cryogenic three-point bending, with 210°C printed samples in supplementary material. Defects are highlighted through SEM-BSE magnification.

Table 4. Results of the Two-way ANOVA for Green Density of Printed Samples.

Source of Variation	Degrees of Freedom	Sum Sq	Mean Sq	P Value
Temperature	2	5.88	8.78	5.65e-4
Feedstock	3	8.38	8.33	1.46e-4
Temperature: Feedstock	6	15.18	7.55	9.89e-6
Residuals	48	16.09		

The PP/PP-MA ratio significantly influences relative density and its temperature-dependent variability. The relative green densities of the printed samples, presented in Figure 4 ,show that while M4-P samples faced significant green density fluctuations due to their high PP/PP-MA and TPE content, M2-P, with a lower PP/PP-MA ratio, showed better performance and stability. This difference is attributed to the M2-P feedstock's improved powder and polymer matrix compatibility, minimizing issues like material dragging and nozzle sticking, hence ensuring more accurate material deposition and print line solidification. The variability in the M4-P feedstock is a result of reduced interaction between the powder surfaces and the polymer matrix, causing material dragging and inaccurate placement and solidification of print lines and a material's propensity to stick in the nozzle, leading to material accumulation on the sides of the printed samples.

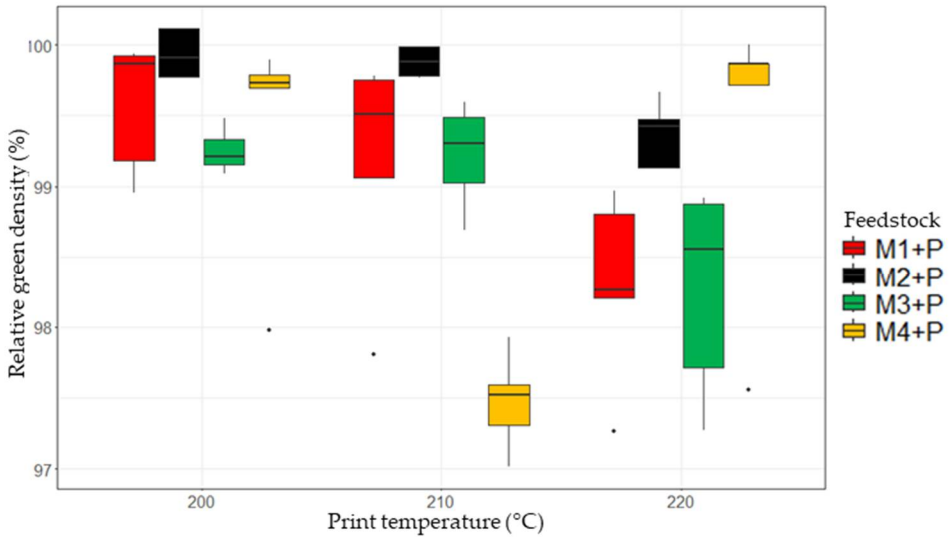

Figure 4. Relative green densities for different feedstocks and printing temperatures.

The cryogenic fracture enabled the identification of various defects within the printed samples, some of which were influenced by the printing temperature. In contrast, others stemmed from the specific feedstock used. All samples exhibited excess material when printed at 220°C, which led to accumulation in the lower side areas of the samples, as shown in Figure 5 b, d, f, h being more notary in samples with high TPE content. Conversely, two main types of defects were more frequently observed at 200°C: the "mountain-type" defect, resulting from material overflow from one print layer to another, creating areas of excess that could interfere with the accurate placement or thorough filling of subsequent layers, and gaps in and between infill lines, due to a lack of material to be extruded. These defects, as illustrated in Figures 5-a, c, e, g, may be exacerbated by variability in filament diameter. Still, capacity of each feedstock to minimize "mountain-type" defects or gaps

 doi:10.20944/preprints202405.0642.v1

between infill lines indicates a feedstock-specific response that ultimately influences the green density of the printed samples. Therefore, green density metrics could reliably reflect a feedstock's effectiveness in producing high-quality printed components.

In Figure 4, it's evident that an increase in temperature had a reductive effect on the relative green density of the samples. Furthermore, TGA analysis indicates slight mass loss before 220°C, likely from moisture desorption or low molecular weight polymer chain degradation, leading to gas generation during printing. This may result in gas entrapment within print lines, affecting green density as depicted in Figure 5-b, d, f, h. This suggests that using increased printing temperature to mitigate high viscosities is highly dependent on the thermal stability of the employed feedstock.

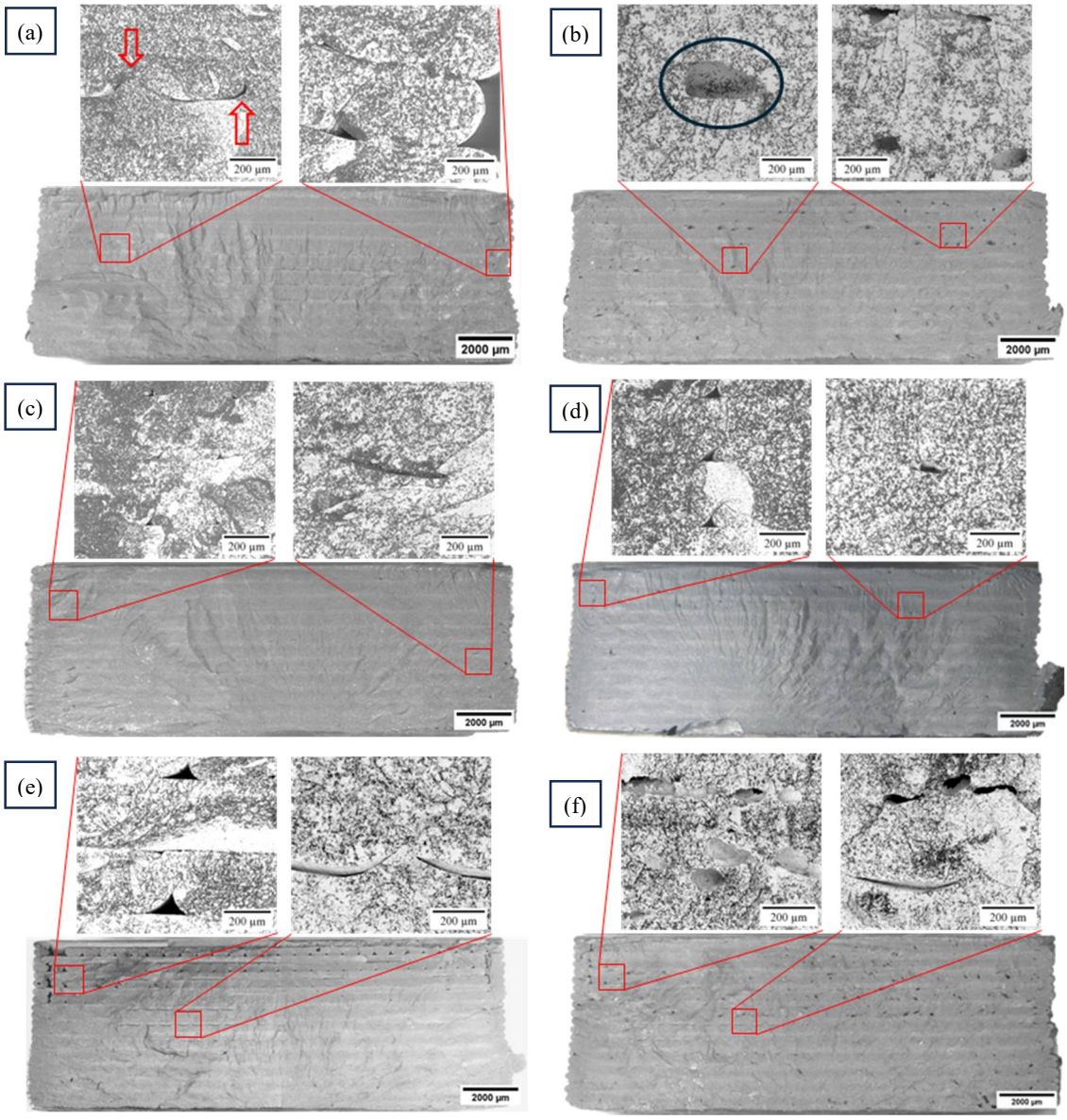

 doi:10.20944/preprints202405.0642.v1

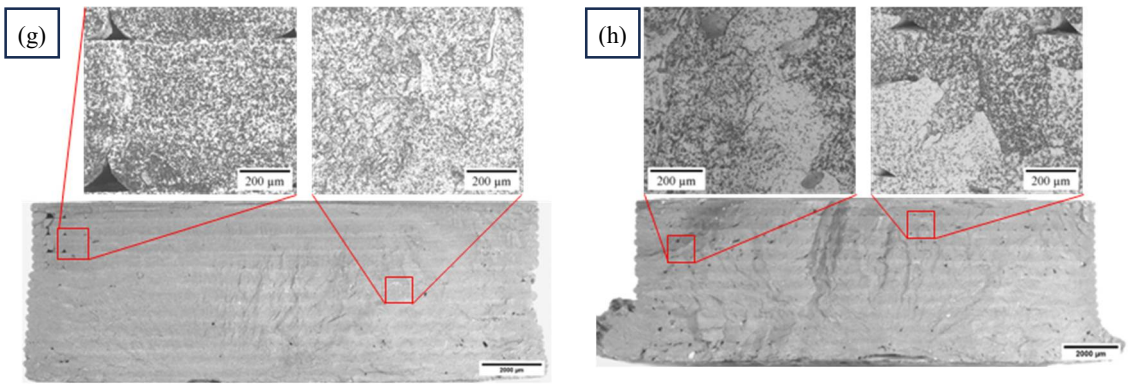

Figure 5. SEM-BSE details and Optical Microscopy of the Green Samples printed at 10 mm/s after cryogenic fracture for the different feedstocks: a), b) M1-P printed at 200°C and 220°C respectively, c), d) M2-P printed at 200°C and 220°C respectively, e), f) M3-P printed at 200°C and 220°C respectively, g), h) M4-P printed at 200°C and 220°C respectively.

3.5. Samples Printed at 7.5 mm/s.

Despite some defects, the superior green density outcomes for all the 200°C printed samples inspired a hypothesis about the impact of printing speed. The findings depicted in Figure 3-a showed that a slower speed of 7.5 mm/s significantly reduced the printing force, implying a quicker attainment of this force level and a shorter delay in material output. Additionally, a reduced printing speed may allow more time for the material to fill the voids identified in samples printed at a faster speed of 10 mm/s. After printing, the cryogenic fracture of the samples was made. See Figure 6. The size and quantity of defects were reduced indicating a positive effect of the printing speed. However, a two-way ANOVA test indicated no significant impact of printing speed on green density outcomes for samples printed at 200°C (see Table 5) due to data dispersion and the challenge of achieving densities near the theoretical 100%, as can be observed in Figure 7-a. Notably, a significant interaction between speed and feedstock was observed, particularly with M4-P samples, which encountered more pronounced adhesion issues at lower speeds, highlighting increased material adhesion in the nozzle and the worsening of material dragging.

Table 5. Results of the Two-way ANOVA for green density of printed Samples at different feedstocks and velocity.

Source of Variation	Degrees of Freedom	Sum Sq	Mean Sq	P Value
Velocity	1	0.156	0.1563	0.32372
Feedstock	3	2.183	0.7277	0.00806
Velocity: Feedstock	3	1.372	0.4572	0.04800
Residuals	32	4.978	0.1556	

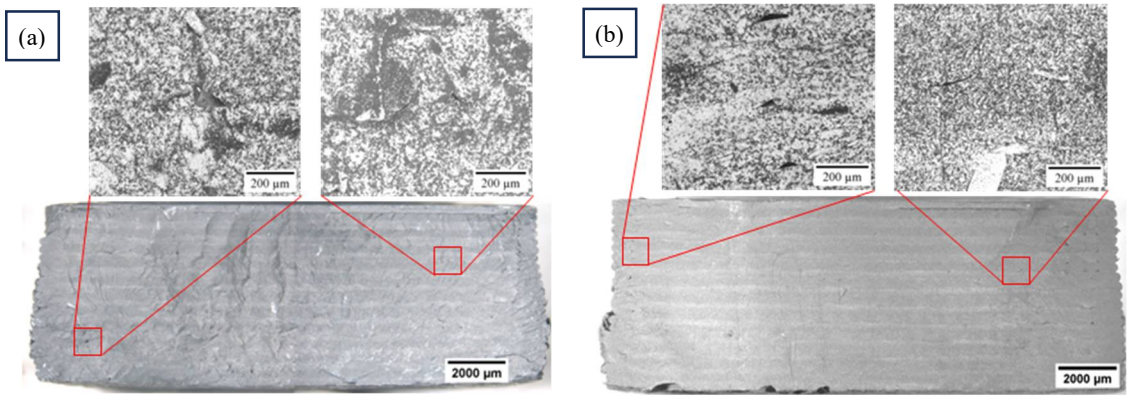

 doi:10.20944/preprints202405.0642.v1

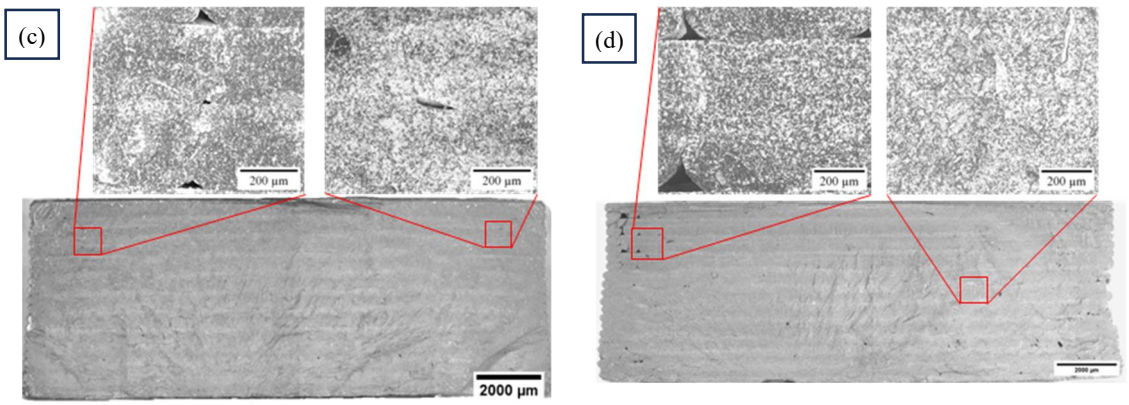

Figure 6. SEM-BSE details and Optical Microscopy of the green samples printed at 7.5 mm/s after cryogenic fracture for the different feedstocks: a) M1-P, a) M2-P, a) M3-P, a) M4-P.

3.5. Sintered Samples.

No clear relationship was found between the green and sintered relative densities. The relative sintered density illustrated in Figure 7-b highlights significant differences in densities and variances. Although the M1-P sample didn't have the highest green density, its higher PP-MA content led to improved sintered density, suggesting two different hypotheses, or an interaction between them, to be tested in the future: a better initial powder dispersion may benefit early sintering stages or low crystallinity feedstocks have a higher swelling effect causing internal defects during solvent debinding. Further studies are needed to validate or reject these hypotheses. Conversely, M2-P feedstock with high green density showed significant variation in sintered density, indicating that these density values are questionable without an optimized solvent debinding and thermal debinding curve. For optimal results, the debinding process must be developed for each feedstock.

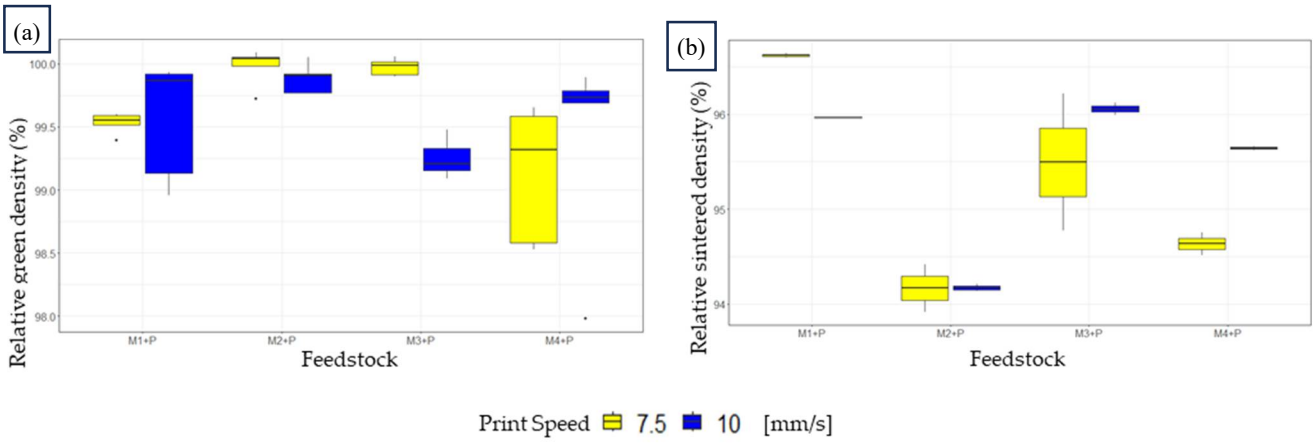

Figure 7. Relative densities of the samples printed at 200°C at different speeds, a) Green state, b) after sintering.

The SEM micrographs of the sintered samples printed at 200°C are depicted in Figure 8. All microstructures exhibit zones of carbon precipitation in the Co matrix, and this can be explained by carbon excess from the polymeric chains' degradation of the backbone, which reduces the measured density of the sintered samples. A reductive atmosphere in thermal debinding will be required to remove this excess carbon [32]. The WC particles in the sintered samples showcase typical faceted structures characteristic of Liquid Phase Sintering [44], along with abnormal grain growth due to the absence of grain growth inhibitors. This observation underscores the necessity of optimizing the sintering cycle for components fabricated through FFF to enhance their microstructural properties [45]. The absence of noticeable Co segregation or WC distribution issues in the microstructure

 doi:10.20944/preprints202405.0642.v1

suggests that adjusting the polymeric raw materials for feedstock improvement is feasible without negatively impacting the microstructural integrity. This opens possibilities for refining the feedstock formulation to enhance the printing process and the final properties of the printed parts.

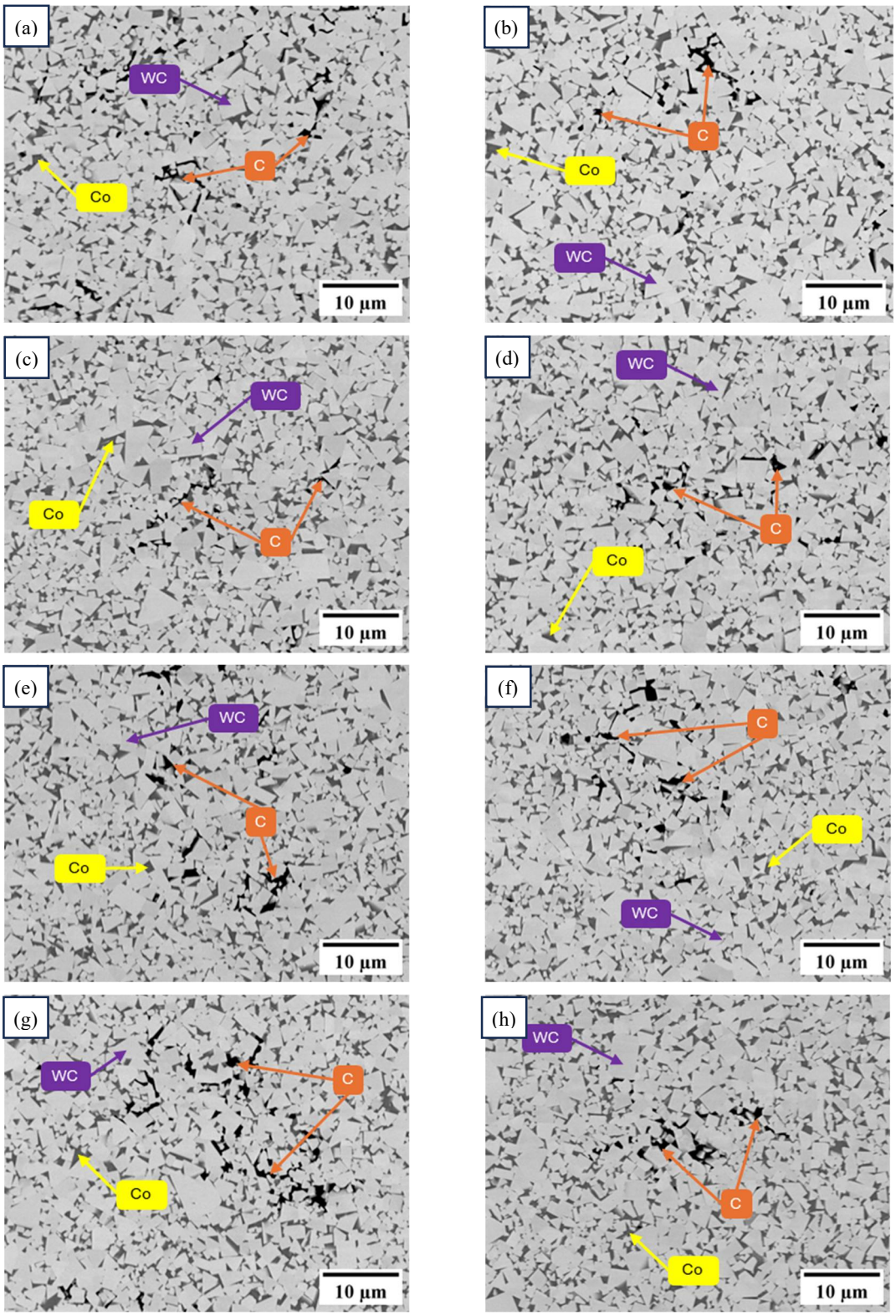

Figure 8. Backscattered SEM micrographs of the sintered samples printed at 200°C made with the developed feedstocks, centered in the carbon precipitated areas printed ad different speeds a) M1-P at 10 mm/s, b) M1-P at 7.5 mm/s, c) M2-P at 10 mm/s, d) M2-P at 7.5 mm/s, e) M3-P at 10 mm/s, f) M3-P at 7.5 mm/s, g) M4-P at 10 mm/s, h) M4-P at 7.5 mm/s.

 doi:10.20944/preprints202405.0642.v1

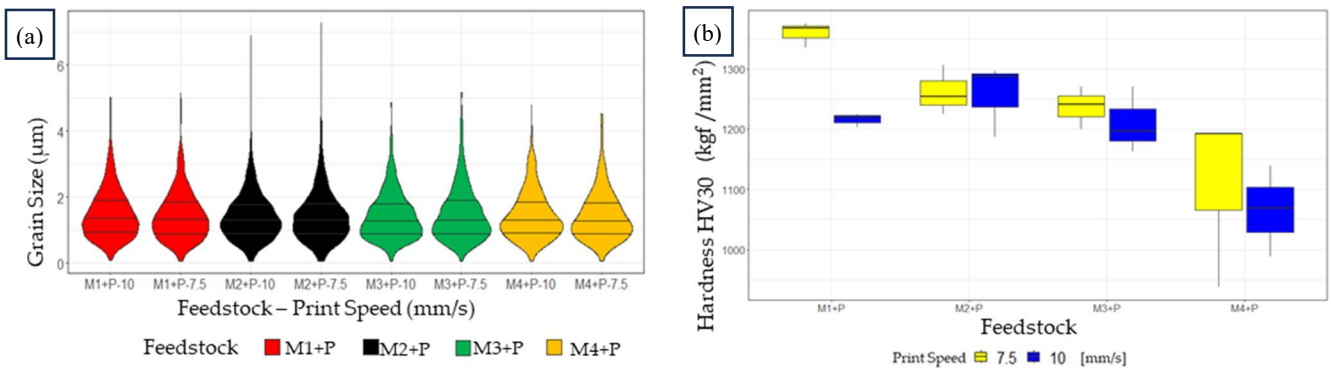

Figure 9. Developed feedstocks after printing at 200°C and sintering at 1500°C a) Violin-plot of grain size from data obtained with digital image processing, b) Vickers hardness.

The formulated feedstocks were diverse in raw polymeric materials. Still, the microstructures displayed only minor variations in WC grain size and distribution, with mean values between 1.42 and 1.48 µm (refer to Figure 9-a) reflecting a minor influence of the formulated binder systems. Only the M2-P feedstock tended to develop more considerable abnormal grain growth. This suggests that the hardness variability noted in Figure 9-b could be attributed to subsurface macro defects. This finding supports the notion that tailored thermal debinding curves are essential for each feedstock developed and that the printing defects in the green state must be avoided.

A two-way ANOVA (Table 6) on hardness response highlighted the significant impact of printing speed, unlike green density, underscoring the critical balance between layer adhesion and defect avoidance for successful debinding and sintering of the parts. Printing defects observed in Figures 10-a, b ,c are examples of how a defect formed in the printing stage, remains post-sintering, with a notable rounding-effect primarily due to the capillary forces of liquid cobalt. This phenomenon causes defects with a low form factor, like those shown in Figure 10-a, to increase in height, negatively impacting the density of the sintered material and, consequently, its mechanical properties. This phenomenon suggests that cracks or defects formed during the solvent or thermal debinding process could worsen during sintering due to capillary force deformation.

Table 6. Results of the Two-way ANOVA for sintered density of the samples printed at 200°C.

Source of Variation	Degrees of Freedom	Sum Sq	Mean Sq	P Value
Velocity	1	17672	3.782	0.0696
Feedstock	3	47619	10.192	0.0005
Velocity: Feedstock	3	5685	1.217	0.3358
Residuals	16	4672		

The findings from this study pave the way for future research focused on optimizing WC-10Co feedstocks and conducting comprehensive analyses of solvent and thermal debinding processes.

 doi:10.20944/preprints202405.0642.v1

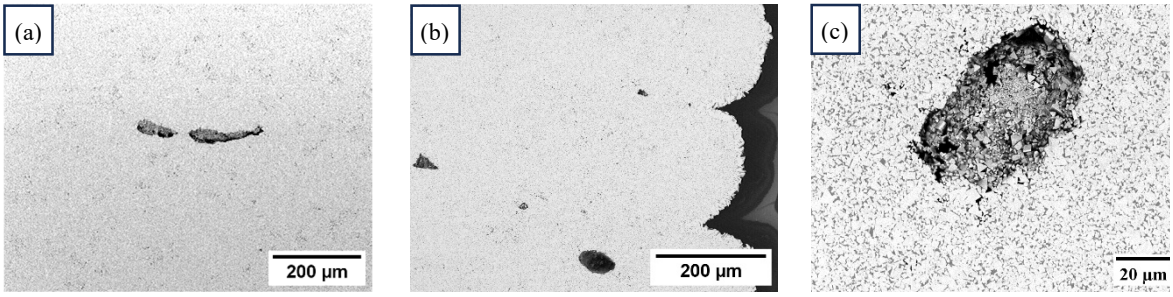

Figure 10. Persistence of printing defects after the sintering process: a) mountain-like defect found in M2-P feedstock, b) Lack of filling between internal infill lines and the outer layer found in M4-P Feedstock, c) Entrapped gas found in M3-P feedstock.

5. Conclusions

Four distinct feedstocks were developed and assessed for their performance in Fused Filament Fabrication of WC-10Co samples. This research paves the way for future studies to refine depolymerization and sintering pathways, establishing a foundational understanding of the importance of feedstock and green sample. The main findings of this study were:

Feedstocks exhibiting lower printing forces tended to develop more defects, which typically persisted through the liquid phase sintering process. Enhancing the ratio of PP-MA to PP within the feedstock improved this situation by facilitating better interaction between the particle surfaces and the binder. This adjustment effectively reduced the melting feedstock's tendency to stick to the printing nozzle, thus mitigating the formation of printing defects.

An increased presence of PP-MA was not directly linked to a significant rise in printing force. Yet, it had a noticeable effect on the mechanical properties of the sintered hard metal. This highlights the importance of a binder system compatible with the powder surface in influencing the outcomes of the sintering process. Future efforts in feedstock formulation will focus on increasing PP-MA content within the binder system to enhance feedstock performance. However, it's crucial to understand that each specific feedstock will necessitate a customized thermal debinding curve. This tailored approach is vital to preventing defect formation during polymer degradation and optimizing the sintered density of the samples, ensuring the successful application of these materials in the FFF manufacturing processes.

The approach for measuring printing force proved to be a quick, cost-effective, and efficient method for rapidly validating different feedstock formulations. However, it necessitates additional efforts to accurately correlate the force response with rheological properties, ensuring that the method's effectiveness extends beyond preliminary assessments to provide a more comprehensive understanding of material behavior. Additionally, adjusting printing speed was found to be a more effective method for reducing printing force than increasing the printing temperature. This adjustment significantly impacts the mechanical properties of the printed parts, highlighting the need for a balance to minimize defects while maximizing final density and hardness.

Author Contributions: Conceptualization, J.D.R.B; methodology, J.D.R.B; software, J.D.R.B; validation, J.D.R.B, A.F.G.P, L.K.H,Q and L.A.B.M; formal analysis, J.D.R.B; investigation, J.D.R.B, A.F.G.P; resources, A.F.G.P, L.K.H,Q and L.A.B.M; data curation, J.D.R.B; writing—original draft preparation, J.D.R.B; writing—review and editing, J.D.R.B, A.F.G.P, L.K.H,Q and L.A.B.M; visualization, J.D.R.B; supervision, L.K.H,Q and L.A.B.M; project administration, L.K.H,Q; funding acquisition, L.K.H,Q.

Funding: The authors thank the Powder Metallurgy Laboratory of "Universidad Nacional de Colombia Sede Bogota", and the "Centro de Materiales y Ensayos of SENA, Regional Distrito Capital", for the logistical, technical, human and financial support of the project. The project funded this research:: "Technological development for the manufacture of metal tools using additive manufacturing techniques based on extrusion for high temperature and wear applications used by the Colombian auto parts industry", code 82305 with contingent recovery financing contract number 2021-1012 of 2021 celebrated between the Colombian institute of educational credit and technical studies abroad "Mariano Ospina Pérez" - ICETEX, the Ministry of Science, Technology and Innovation and the National University of Colombia

 doi:10.20944/preprints202405.0642.v1

Conflicts of Interest: The authors declare no conflicts of interest.

References

1. Mahmoodan, M.; Aliakbarzadeh, H.; Gholamipour, R. Sintering of WC-10%Co Nano Powders Containing TaC and VC Grain Growth Inhibitors. *Trans. Nonferrous Met. Soc. China (English Ed.* **2011**, *21*, 1080–1084, doi:10.1016/S1003-6326(11)60825-X.
2. Farag, S.; Konyashin, I.; Ries, B. The Influence of Grain Growth Inhibitors on the Microstructure and Properties of Submicron, Ultrafine and Nano-Structured Hardmetals – A Review. *Int. J. Refract. Met. Hard Mater.* **2018**, *77*, 12–30, doi:10.1016/j.ijrmhm.2018.07.003.
3. Rubiano Buitrago, J.D.; Gil Plazas, A.F.; Herrera Quintero, L.K. Influence of TiC and Cr3C2 Additions on the Mechanical Properties of a (W-Ti-Cr)C-Co Sintered Hardmetal. *J. Mater. Res. Technol.* **2019**, *8*, doi:10.1016/j.jmrt.2019.09.042.
4. Upadhyaya, G.S. Classification and Applications of Cemented Carbides. In *Cemented Tungsten Carbides*; William Andrew Publishing: Westwood, NJ, 1998; pp. 288–308 ISBN 978-0-8155-1417-6.
5. Quinlan, H.E.; Hasan, T.; Jaddou, J.; Hart, A.J. Industrial and Consumer Uses of Additive Manufacturing: A Discussion of Capabilities, Trajectories, and Challenges. *J. Ind. Ecol.* **2017**, *21*, S15–S20, doi:10.1111/jiec.12609.
6. Xiong, Y.; Smugeresky, J.E.; Schoenung, J.M. The Influence of Working Distance on Laser Deposited WC-Co. *J. Mater. Process. Technol.* **2009**, *209*, 4935–4941, doi:10.1016/j.jmatprotec.2009.01.016.
7. Li, Y.; Bai, P.; Wang, Y.; Hu, J.; Guo, Z. Effect of Ni Contents on the Microstructure and Mechanical Properties of TiC-Ni Cermets Obtained by Direct Laser Fabrication. *Int. J. Refract. Met. Hard Mater.* **2009**, *27*, 552–555, doi:10.1016/j.ijrmhm.2008.07.006.
8. Zong, G.; Wu, Y.; Tran, N.; Lee, I.; Bourell, D.L.; Beaman, J.J.; Marcus, H.L. Direct Selective Laser Sintering of High Temperature Materials. *Proc. Solid Free. Fabr. Symp.* **1992**, 72–85.
9. Kumar, S.; Czekanski, A. Optimization of Parameters for SLS of WC-Co. *Rapid Prototyp. J.* **2017**, *23*, 1202–1211, doi:10.1108/RPJ-10-2016-0168.
10. Uhlmann, E.; Bergmann, A.; Bolz, R.; Gridin, W. Application of Additive Manufactured Tungsten Carbide Tool Electrodes in EDM. *Procedia CIRP* **2018**, *68*, 86–90, doi:10.1016/j.procir.2017.12.027.
11. Vaezi, M.; Drescher, P.; Seitz, H. Beamless Metal Additive Manufacturing. *Materials (Basel).* **2020**, *13*, doi:10.3390/ma13040922.
12. Gonzalez-Gutierrez, J.; Cano, S.; Schuschnigg, S.; Kukla, C.; Sapkota, J.; Holzer, C. Additive Manufacturing of Metallic and Ceramic Components by the Material Extrusion of Highly-Filled Polymers: A Review and Future Perspectives. *Materials (Basel).* **2018**, *11*, doi:10.3390/ma11050840.
13. Aramian, A.; Razavi, S.M.J.; Sadeghian, Z.; Berto, F. A Review of Additive Manufacturing of Cermets. *Addit. Manuf.* **2020**, *33*, 101130, doi:10.1016/j.addma.2020.101130.
14. Leary, M. *Directed Energy Deposition*; 2020; ISBN 9780128167212.
15. S. Scott APPARATUS AND METHOD FOR CREATING THREE-DIMENSIONAL OBJECTS. *Bunseki Kagaku* 1992, *28*, 195–196.
16. Sells, E.; Bailard, S.; Smith, Z.; Bowyer, A.; Olliver, V. RepRap: The Replicating Rapid Prototyper: Maximizing Customizability by Breeding the Means of Production. *Handb. Res. Mass Cust. Pers.* **2009**, 568–580, doi:10.1142/9789814280280_0028.
17. Kukla, C.; Gonzalez-gutierrez, J.; Cano, S.; Hampel, S. Fused Filament Fabrication (FFF) of PIM Feedstocks. *Proc. VI Congr. Nac. Pulvimetalurgia y I Congr. Iberoam. Pulvimetalurgia* **2017**.
18. Suwanpreecha, C. A Review on Material Extrusion Additive Manufacturing of Metal and How It Compares with Metal Injection Moulding. **2022**.
19. Agarwala, M.K.; Bandyopadhyay, A.; Van Weeren, R. Fused Deposition of Ceramics (FDC) for Structural Silicon Nitride Components. *Proc. Solid Free. Fabr. Symp.* **1996**, 336–344.
20. Agarwala, M.K.; Weeren, R. Van; Bandyopadhyay, A.; Safari, A.; Danforth, S.C.; Priedeman, W.R. Filament Feed Materials for Fused Deposition Processing of Ceramics and Metals. In Proceedings of the Proceedings ofthe Solid Freeform Fabrication Symposium; 1996; pp. 451–458.
21. Venkataraman, N.; Rangarajan, S.; Matthewson, M.J.; Harper, B.; Safari, A.; Danforth, S.C.; Wu, G.; Langrana, N.; Guceri, S.; Yardimci, A. Feedstock Material Property - Process Relationships in Fused Deposition of Ceramics (FDC). *Rapid Prototyp. J.* **2000**, *6*, 244–252, doi:10.1108/13552540010373344.
22. Hwang, K.S.; Lin, H.K.; Lee, S.C. Thermal, Solvent, and Vacuum Debinding Mechanisms of PIM Compacts. *Mater. Manuf. Process.* **1997**, *12*, 593–608, doi:10.1080/10426919708935169.
23. Kukla, C.; Cano, S.; Kaylani, D.; Schuschnigg, S.; Holzer, C.; Gonzalez-Gutierrez, J. Debinding Behaviour of Feedstock for Material Extrusion Additive Manufacturing of Zirconia. *Powder Metall.* **2019**, *62*, 196–204, doi:10.1080/00325899.2019.1616139.
24. Elkins, K.; Nordby, H.; Janak, C.; Gray, R.W.; Bohn, J.H.; Baird, D.G. Soft Elastomers for Fused Deposition Modeling. In Proceedings of the Solid Freeform Fabrication Proceedings, September 1997; 1997; pp. 441–448.

25. Gil-Plazas, A.-F., Rubiano-Buitrago, J.-D., Boyacá-Mendivelso, L.-A., & Herrera-Quintero, L.-K. Solid-State and Super Solidus Liquid Phase Sintering of 4340 Steel SLM Powders Shaped by Fused Filament Fabrication. *Rev. Fac. Ing.* **2022**, *31*, e13913, doi:https://doi.org/10.19053/01211129.v31.n60.2022.13913.
26. Godec, D.; Cano, S.; Holzer, C.; Gonzalez-Gutierrez, J. Optimization of the 3D Printing Parameters for Tensile Properties of Specimens Produced by Fused Filament Fabrication of 17-4PH Stainless Steel. *Materials (Basel).* **2020**, *13*, doi:10.3390/ma13030774.
27. Coelho, S.; Magro, A.; Texeira, P.; Ferreira, N.; Pereira, P.; Rodrigues, F.; Jorge, H.; Sacramento, J. Development of Formulations of WC-Co Filament for Fused Filament Fabrication.; 2020.
28. Cano, S.; Gonzalez-Gutierrez, J.; Sapkota, J.; Spoerk, M.; Arbeiter, F.; Schuschnigg, S.; Holzer, C.; Kukla, C. Additive Manufacturing of Zirconia Parts by Fused Filament Fabrication and Solvent Debinding: Selection of Binder Formulation. *Addit. Manuf.* **2019**, *26*, 117–128, doi:10.1016/j.addma.2019.01.001.
29. McNulty, T.F.; Mohammadi, F.; Bandyopadhyay, A.; Shanefield, D.J.; Danforth, S.C.; Safari, A. Development of a Binder Formulation for Fused Deposition of Ceramics. *Rapid Prototyp. J.* **1998**, *4*, 144–150, doi:10.1108/13552549810239012.
30. Cano, S.; Gooneie, A.; Kukla, C.; Rieb, G.; Holzer, C.; Gonzalez-Gutierrez, J. Modification of Interfacial Interactions in Ceramic-Polymer Nanocomposites by Grafting: Morphology and Properties for Powder Injection Molding and Additive Manufacturing. *Appl. Sci.* **2020**, *10*, doi:10.3390/app10041471.
31. Momeni, V.; Shahroodi, Z.; Gonzalez-Gutierrez, J.; Hentschel, L.; Duretek, I.; Schuschnigg, S.; Kukla, C.; Holzer, C. Effects of Different Polypropylene (PP)-Backbones in Aluminium Feedstock for Fused Filament Fabrication (FFF). *Polymers (Basel).* **2023**, *15*, doi:10.3390/polym15143007.
32. Lengauer, W.; Duretek, I.; Fürst, M.; Schwarz, V.; Gonzalez-Gutierrez, J.; Schuschnigg, S.; Kukla, C.; Kitzmantel, M.; Neubauer, E.; Lieberwirth, C.; et al. Fabrication and Properties of Extrusion-Based 3D-Printed Hardmetal and Cermet Components. *Int. J. Refract. Met. Hard Mater.* **2019**, *82*, 141–149, doi:10.1016/j.ijrmhm.2019.04.011.
33. Mukesh K. Agarwala; Vikram R. Jamalabad; Noshir A. Langrana; Ahmad Safari; Philip J. Whalen and; Stephen C. Danforth Structural Quality of Parts Processed by Fused Deposition. *Rapid Prototyp. J.* **1996**, *2*, 4–19.
34. Agarwala, M.K.; Weeren, R. Van; Bandyopadhyayl, A.; Whalen, P.J.; Safari, A.; Danforth, S.C. Fused Deposition of Ceramics and Metals : An Overview. In Proceedings of the Proceedings of Solid Freeform Fabrication Symposium; 1996; pp. 385–392.
35. Fayyaz, A.; Muhamad, N.; Sulong, A.B.; Yunn, H.S.; Amin, S.Y.M.; Rajabi, J. Micro-Powder Injection Molding of Cemented Tungsten Carbide: Feedstock Preparation and Properties. *Ceram. Int.* **2015**, *41*, 3605–3612, doi:10.1016/j.ceramint.2014.11.022.
36. Yang, M.J.; German, R.M. Nanophase and Superfine Cemented Carbides Processed by Powder Injection Molding. *Int. J. Refract. Met. Hard Mater.* **1998**, *16*, 107–117, doi:10.1016/S0263-4368(98)00016-X.
37. Percoco, G.; Arleo, L.; Stano, G.; Bottiglione, F. Analytical Model to Predict the Extrusion Force as a Function of the Layer Height, in Extrusion Based 3D Printing. *Addit. Manuf.* **2021**, *38*, 101791, doi:10.1016/j.addma.2020.101791.
38. Mbow, M.M.; Marin, P.R.; Pourroy, F. Extruded Diameter Dependence on Temperature and Velocity in the Fused Deposition Modeling Process. *Prog. Addit. Manuf.* **2020**, *5*, 139–152, doi:10.1007/s40964-019-00107-4.
39. Tarani, E.; Arvanitidis, I.; Christofilos, D.; Bikiaris, D.N.; Chrissafis, K.; Vourlias, G. Calculation of the Degree of Crystallinity of HDPE/GNPs Nanocomposites by Using Various Experimental Techniques: A Comparative Study. *J. Mater. Sci.* **2023**, *58*, 1621–1639, doi:10.1007/s10853-022-08125-4.
40. Wunderlich, B. *Thermal Analysis of Polymeric Materials*; Springer-Verlag: Berlin/Heidelberg, 2005; ISBN 3-540-23629-5.
41. Gonzalez-Gutierrez, J.; Duretek, I.; Kukla, C.; Poljšak, A.; Bek, M.; Emri, I.; Holzer, C. Models to Predict the Viscosity of Metal Injection Molding Feedstock Materials as Function of Their Formulation. *Metals (Basel).* **2016**, *6*, doi:10.3390/met6060129.
42. Singh, P.; Balla, V.K.; Tofangchi, A.; Atre, S. V.; Kate, K.H. Printability Studies of Ti-6Al-4V by Metal Fused Filament Fabrication (MF3). *Int. J. Refract. Met. Hard Mater.* **2020**, *91*, 105249, doi:10.1016/j.ijrmhm.2020.105249.
43. Ghasemi-Mobarakeh, L.; Cano, S.; Momeni, V.; Liu, D.; Duretek, I.; Riess, G.; Kukla, C.; Holzer, C. Effect of Increased Powder–Binder Adhesion by Backbone Grafting on the Properties of Feedstocks for Ceramic Injection Molding. *Polymers (Basel).* **2022**, *14*, doi:10.3390/polym14173653.
44. German, R.M.; Suri, P.; Park, S.J. Review: Liquid Phase Sintering. *J. Mater. Sci.* **2009**, *44*, 1–39, doi:10.1007/s10853-008-3008-0.
45. García, J.; Collado Ciprés, V.; Blomqvist, A.; Kaplan, B. Cemented Carbide Microstructures: A Review. *Int. J. Refract. Met. Hard Mater.* **2019**, *80*, 40–68, doi:10.1016/j.ijrmhm.2018.12.004.

 doi:10.20944/preprints202405.0642.v1